Materials Research Express

INCLUSIVE PUBLISHING
TRUSTED SCIENCE

PAPER • OPEN ACCESS

Enhancing plasticity of ‘self-sharpening’ tungsten high-entropy alloy via tailoring *μ*-precipitation

To cite this article: Tong Li *et al* 2023 *Mater. Res. Express* **10** 076511

View the article online for updates and enhancements.

You may also like

- Research on Comprehensive Evaluation Model of Investment Benefits of Transmission and Transformation Projects
Junkai Ge, Xiaoyu Xu, Wenhan Chen et al.
- Integral transformations applied to image encryption
Juan M. Vilardy, Ronal Perez and Cesar O. Torres
- Application Analysis of Virtualization Technology Based on General Server Small Cell
Dalin Zhao

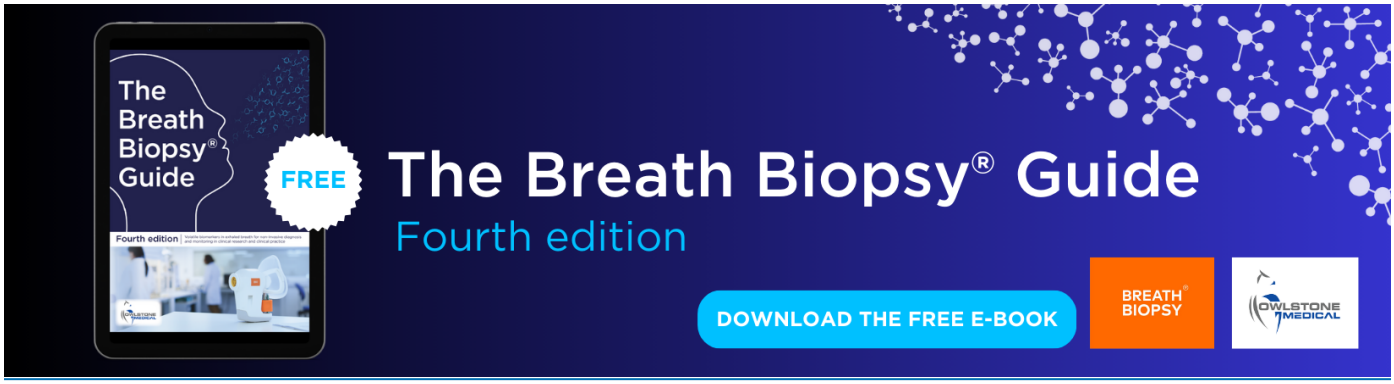

This content was downloaded from IP address 159.226.200.166 on 12/04/2024 at 08:14

Materials Research Express

PAPER

Enhancing plasticity of 'self-sharpening' tungsten high-entropy alloy via tailoring μ-precipitation

Tong Li[1,2], **Jinxi Chen**[1,2], **Feng Chen**[1,2], **Yan Chen**[1,2] **and Lanhong Dai**[1,2,*]

[1] State Key Laboratory of Nonlinear Mechanics, Institute of Mechanics, Chinese Academy of Sciences, Beijing 100190, People's Republic of China
[2] School of Engineering Science, University of Chinese Academy of Sciences, Beijing 101408, People's Republic of China
[*] Author to whom any correspondence should be addressed.

E-mail: lhdai@lnm.imech.ac.cn

Keywords: high-entropy alloys, precipitation, phase transformation, plasticity

OPEN ACCESS

RECEIVED
12 April 2023

REVISED
25 June 2023

ACCEPTED FOR PUBLICATION
12 July 2023

PUBLISHED
20 July 2023

Original content from this work may be used under the terms of the Creative Commons Attribution 4.0 licence.

Any further distribution of this work must maintain attribution to the author(s) and the title of the work, journal citation and DOI.

Abstract

In our recently published work (Acta Materialia 186 (2020) 257–266), we have designed a new equimolar tungsten high-entropy alloy with excellent penetration ability to satisfy the highly desirable of 'self-sharping' in wide range of engineering application. This alloy has outstanding dynamic compressive properties and superior penetration performance than that of 93 W alloys. In this work, the tension properties of the tungsten high-entropy alloy were significantly improved by μ phase precipitation design strategy to tailor the morphology and distribution of μ phase. Through controlling the phase transformation process, the μ phase changes from liquid-solid phase transformation to solid-solid precipitation phase transformation. This can effectively impede the brittleness caused by the μ phase segregation at the grain boundary and phase boundary. Moreover, the Orowan effect caused by nano-sized μ-phase particles improves the tensile strength effectively (enhancing ~150%) and ensure the ductility. This material design strategy significantly improves the tension ductility of the alloy and provides a new paradigm to solve the similar problem of material brittleness.

1. Introduction

Materials with high performance of self-sharping are highly required in wide range of penetration engineering application [1–3]. Among the traditional alloys, only depleted uranium alloys exhibit self-sharpening properties [4], but they have the problem of environmental contamination [5]. Fortunately, a emerging design paradigm of alloys with multiple-principal-element, often termed as high-entropy alloys (HEAs), has presented promising pathways for seeking new and improved alloys within a previously unexplored compositional/phase space [6–16]. Based on the average valence electron concentration strategy, a novel equimolar WMoFeNi high-entropy alloy with excellent self-sharpening properties has been successfully developed in our previous work [3]. Owing to the unique microstructure composition of body-centered cubic (BCC), face-centered cubic (FCC), and rhombohedral μ phase with topologically close-packed (TCP) structure, a 10%–20% better penetration performance over that of conventional tungsten heavy alloys (93W) was achieved [3]. During penetration, the ultra-strong μ phase induced the high local strain gradient, which generates the emergence of shear band and self-shaping behavior. In addition, WMoFeNi obtain high strength and plasticity during dynamic compressive test. However, in the WMoFeNi high-entropy alloy, μ phase will diverge greatly at grain boundaries and phase boundaries, which leads to the limited tensile ductility and machining property [2, 3]. Thus, improving its plasticity is in pressing need for industrial applications.

In this work, by controlling the phase transformation process, the as-cast μ-phase structure is eliminated and the μ-phase is distributed uniformly as nano-precipitated particle in the matrix. Based on such material design strategy, a post-optimized un-equimolar W30Mo7FeNi high-entropy alloy was prepared. Compared with the equimolar WMoFeNi, the element proportion of Mo is reduced to avoid the appearance of the as-cast μ

© 2023 The Author(s). Published by IOP Publishing Ltd

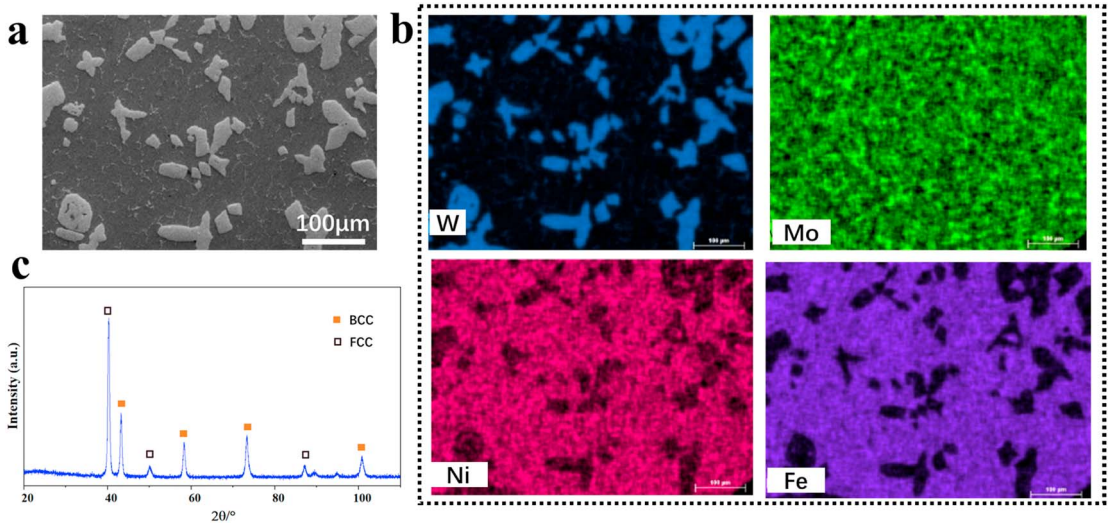

Figure 1. Structural analysis of the as-cast W30Mo7FeNi high-entropy alloy. (a) SEM topography of material. (b) Morphology of element distribution in corresponding region of a. (c). Structure analysis of XRD.

phase. Meanwhile, Mo element is kept in supersaturated solution state in the matrix phase, which provides conditions for the aging precipitation of μ phase.

2. Materials and methods

2.1. Materials

Bulk W30Mo7FeNi ((W30-Mo7-Fe31.5-Ni31.5, in at.%)) alloy samples are prepared by arc melting of counterpart pure metals (purity >99.99%) in Ar atmosphere. After air cooling, the bulk ingots are hot-rolled at 1000 °C with a rolling reduction ratio of 50% and subsequently cold-rolled at room temperature with a reduction ratio of 50%. Following cold rolling, stepwise thermodynamic treatments involving annealing at 1000 °C for 2 min, then aging at 650 °C for 30 h, followed by water quenching.

2.2. Microstructure characterization

Electron back-scattered diffraction (EBSD) measurements were carried out in a field-emission SEM (JEOL–JSM–7001F) equipped with an automatic orientation acquisition system (Oxford Instruments-HKL Channel 5). Specimens were mechanically ground and polished, and then electropolished at room temperature with an electrolyte of 90% ethanol and 10% perchloric acid. Constituent phases in the alloy were identified in an x-ray diffractometer (XRD; Rigaku Dmax 2500) using a CuKα radiation. The microstructures before and after deformation were characterized by scanning electron microscopy (SEM; JSM-7100F) and transmission electron microscopy (TEM; JEM-2100F) at 200 kV.

2.3. Mechanical property evaluation

Dog-bone-shaped specimens for uniaxial tensile testing, with a gauge length of 12.5 mm and a cross-section area of 2.0×0.5 mm^2, were fabricated by electro-discharge machining. Using an MTS-810 servo-hydraulic universal testing machine (MTS Corp., Eden Prairie, MN), uniaxial tensile tests were carried out at room temperature at a constant strain rate of 5×10^{-4} s^{-1}.

3. Results

3.1. Microstructural characteristics

The chemical compositions and microstructure of the as-cast W30Mo7FeNi alloy was characterized by SEM and Energy-dispersive x-ray spectroscopy (EDS) (figures 1(a) and (b)). Table 1 shows the content of each element in BCC and FCC. The dendritic BCC phase distributes in the FCC matrix. It can be observed from the EDS images (figure 1(b)) that the W element in the BCC phase has obvious segregation, while the Fe/Ni element is significantly reduced. These results indicate that the segregation of elements is the main reason for phase separation of BCC and FCC during solidification. Combined with x-ray diffractometer (XRD), the two-phase structure of the material was further analyzed (figure 1(c)). The diffraction peaks of the BCC and FCC structures

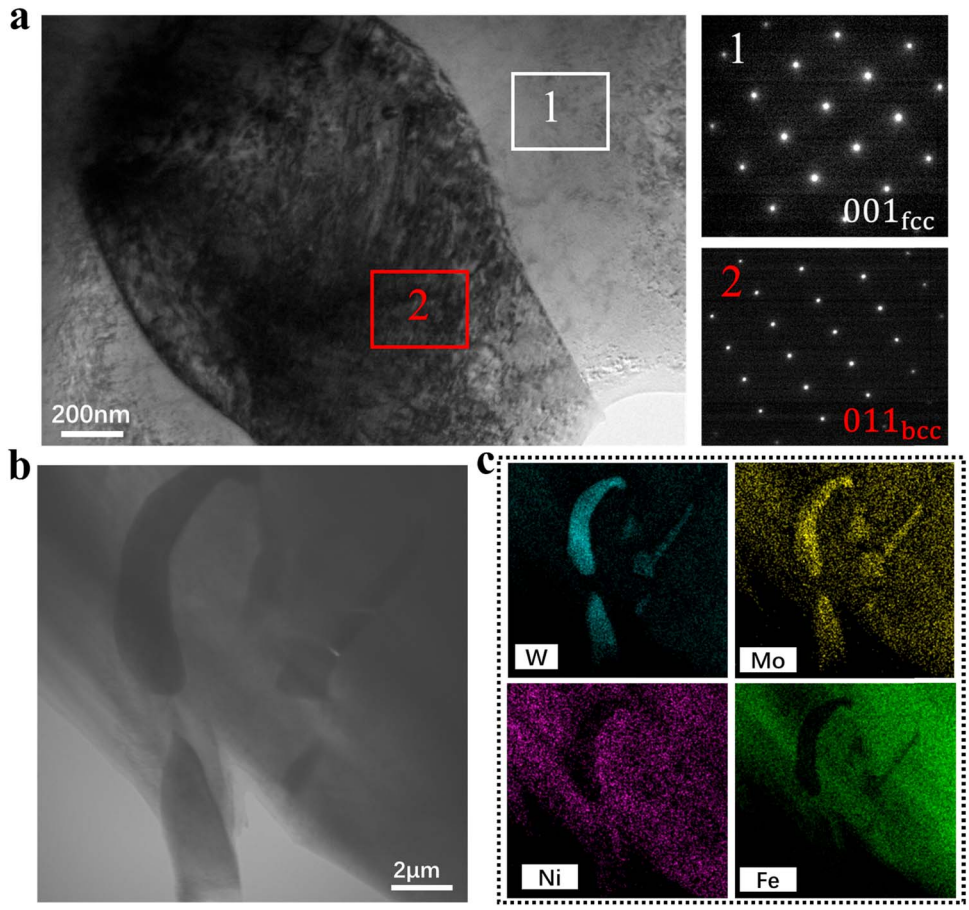

Figure 2. TEM characterization and elements distribution of the as-cast W30Mo7FeNi high-entropy alloy. (a) Bright field TEM image and corresponding SAED patterns. (b) HAADF image of alloy. (c) The corresponding EDS e maps of a show the distribution of different elements.

can be clearly identified. Obviously, the as-cast structure eliminates the μ phase that segregates at the grain boundary and phase boundary by phase tailor.

In order to further analyze the two-phase structure of the as-cast material, the crystallographic structures (figure 2(a)) were characterized by transmission electron microscopy (TEM). By select area electron diffraction (SAED) patterns of the corresponding regions, the lattice constants of BCC and FCC can be determined as 0.28 nm and 0.33 nm. From the bright-field TEM image (figure 2(a)), it clearly shows that BCC and FCC have sharp phase interface, and there is no coherent relationship between the two structures. High-angle annular dark field (HAADF) image (figure 2(b)) and corresponding EDS maps (figure 2(c)) further show the distribution of elements between the two phases. The results clearly show that W/Mo elements are enriched in BCC phase, while Fe/Ni is reduced. The results of TEM analysis were consistent with those of SEM and XRD.

μ phase with TCP structure is the dominated factor of self-sharping ability. Combined with rolling and aging process, μ phase can be precipitated in FCC matrix. The phase structure and grain size changes at different stages in the treatment process are shown in figure 3. The grain size of as-cast W30Mo7FeNi is about 400 μm (figure 3(a)), and the volume fraction of BCC phase and FCC phase is about 30% and 40% (figure 3(b)), respectively. After recrystallization annealing, the grain size of the rolled material was obviously refined. The grain size of FCC phase decreased to about 3 μm, and the recrystallization behavior of BCC phase did not occur (figures 3(c) and (d)). In order to precipitate μ phase, the material was aged at 650 °C for 30 h. It can be observed from the IPF diagram that the grain size of the material did not grow after aging (figures 3(e) and (f)). During the whole process, the BCC structure remained stable. Because of the size of nanometer, μ-phase precipitation cannot be accurately analyzed by EBSD.

Utilizing TEM, the morphology and crystallographic structure of μ phase were carefully analyzed (figure 4). The bright-field TEM image shows that the μ phase is distributed uniformly in the FCC base phase in granular form, with the particle size of about 100–200 nm (figure 4(a)). By the SAED pattern (figure 4(b)), the topologically close-packed structure of μ phase can be characterized as rhombohedral with the lattice parameters

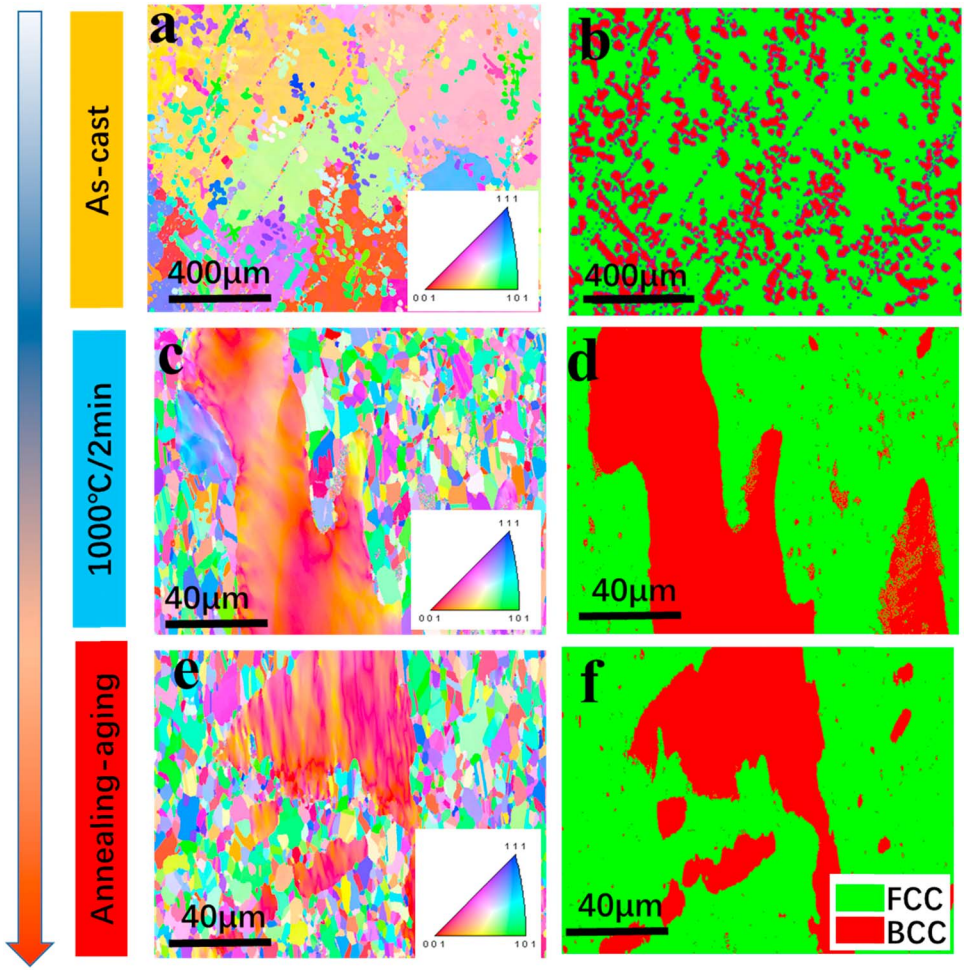

Figure 3. The microstructure evolution of $W_{30}Mo_7FeNi$ high-entropy alloy during rolling and heat-treatment process. (a), (c), (e), are the inverse pole figures (IPFs) of as-cast, annealing, and aging materials, respectively. (b), (d), (f), are the corresponding phase diagrams.

of a = b = 0.475 nm and c = 2.567 nm (space group 166, R3m) [2, 3, 17]. To further analyze the structure of the μ-phase, the atomic arrangement was characterized by high-resolution TEM. Figure 4(c) presents the atomic plane of {0001} and the corresponding fast Fourier transformation (FFT) pattern. It is observed that the atoms are arranged in a hexagonal periodic pattern along {0001} plane, which is consistent with the work we reported before. The compositions of FCC matrix are mainly Fe and Ni and has low stacking fault energy. Therefore, some annealing twins occur during the recrystallization annealing process (figure 4(d)). According to SAED pattern embedded in figure 4(d), the lattice parameters of FCC phase can be calculated as a = b = c = 0.33 nm, which is consistent with that of the as-cast alloy. The elements distribution of μ phase was analyzed by HAADF and the corresponding EDS maps. Figure 4(e) shows that, compared with the FCC matrix, W and Mo are segregated in the μ phase, while Fe and Ni are relatively reduced. This is consistent with our previous study that the content of four elements in the μ phase is close to the equimolar ratio.

3.2. Mechanical properties

Based on the μ phase precipitation control strategy, the mechanical properties of the material are significantly optimized. Dog-bone-shaped tensile sample, shows that the yield strength of the as-cast alloy is ~350 MPa with a fracture strain of ~15% (figure 5(a)). The yield strength of the alloy increased to 950 MPa (2.8 times of that of the as-cast material). Meanwhile, the alloy still maintains good ductility after aging (~8%) (figure 5(a)). Through fracture analysis, it can be seen that ductile fracture and cleavage fracture exist in both the two states of the alloys (figures 5(b) and (c)). The ductile fracture occurred in FCC phase and cleavage fracture occurred in BCC phase. Unlike the equimolar WMoFeNi high-entropy alloy, μ phase is no longer the limiting factor of plasticity. These results indicate that the μ-phase precipitation strategy successfully improves the machinability of the materials.

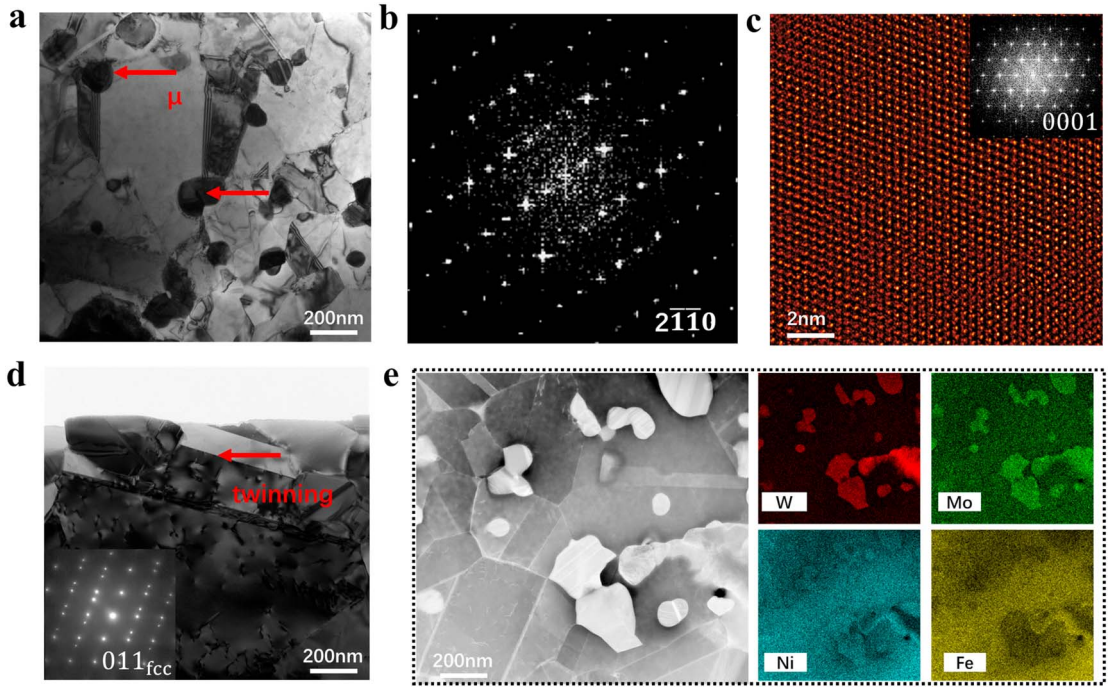

Figure 4. TEM characterization of refined FCC structure and μ phase. a. Bright-field TEM image of μ phase. b. The corresponding SAED pattern along $\langle 2\,\bar{1}\,\bar{1}0\rangle$ zone axis of μ phase. c. The high-resolution TEM image and corresponding fast Fourier transformation (FFT) of μ phase. d. Bright-field TEM image of annealing twin structure in FCC matrix. e. HAADF image of μ phase and the corresponding EDS distribution maps of different elements.

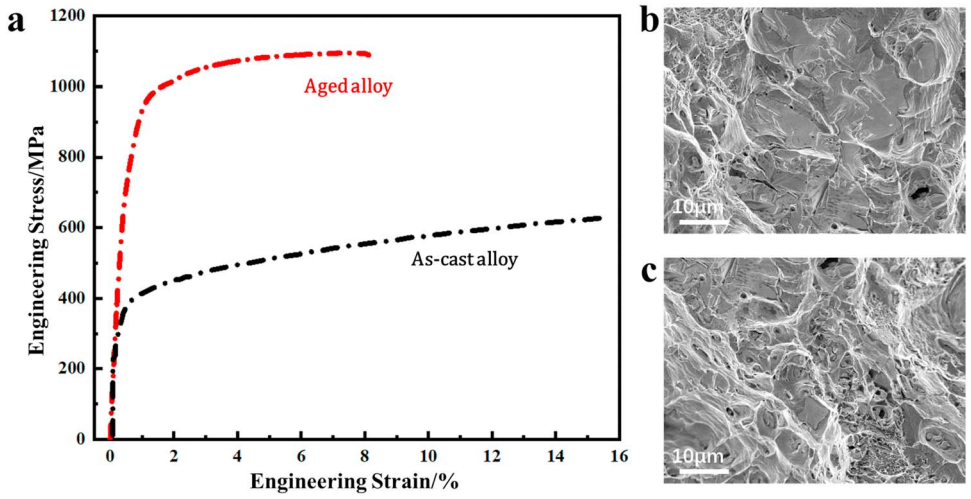

Figure 5. Quasi-static tensile properties and fracture morphology of W30Mo7FeNi high-entropy alloy. (a). Quasi-static tensile curves of as-cast and aged alloys. (b). Fracture morphology of aged alloy. (c). Fracture morphology of as-cast alloy.

Table 1. Compositions of the as-cast W30Mo7FeNi high-entropy alloy (at. %).

Phase	W	Mo	Fe	Ni
BCC	74	18	4	4
FCC	6	7	44	43

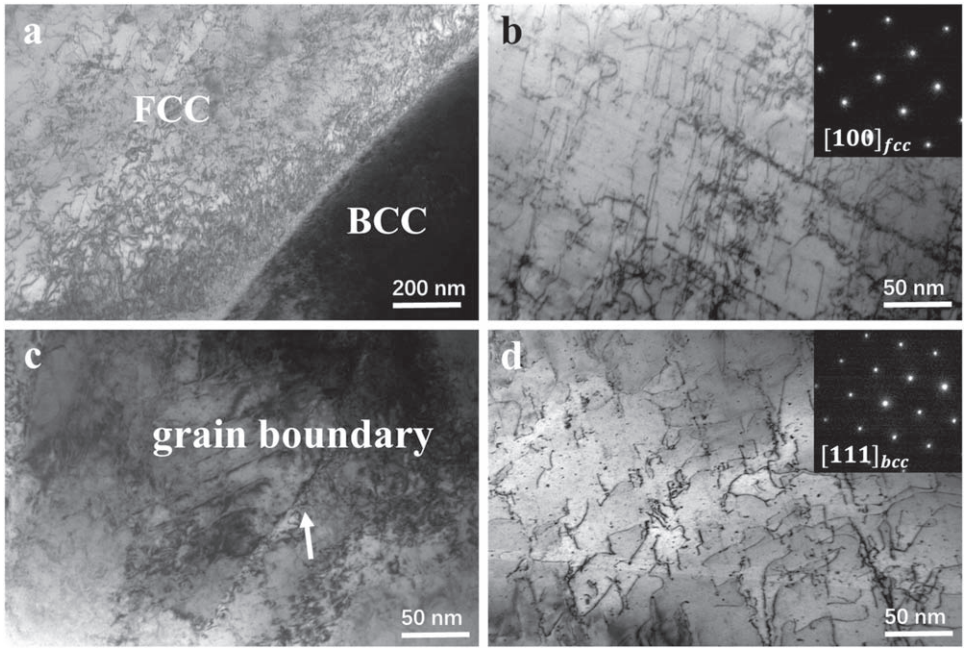

Figure 6. Microstructure of the as-cast alloy after tensile deformation. (a). Bright-field TEM image of dislocations pile at phase boundary. (b). Bright-field TEM image of dislocation slip morphology in FCC and the corresponding SAED pattern. (c). Bright-field TEM image shows that the dislocation pile at grain boundary. (d). Bright-field TEM image of dislocation slip morphology in BCC and the corresponding SAED pattern.

4. Discussion

4.1. The deformation mechanism of the as-cast alloy

In order to analyze the deformation mechanism of the as-cast W30Mo7FeNi high-entropy alloy, the tensile samples were carefully characterized by TEM. Significant work hardening is observed in the tensile stress-strain curves of as-cast alloy, which is owing to the multiplication and evolution of dislocations. As showed in figure 6(a), (a) large number of dislocations accumulate at the FCC and BCC phase boundary, which is a major source of strength for as-cast materials. The dislocation in the FCC matrix is dominated by monophyletic slip (figure 6(b)) and has significantly higher dislocation density than that in BCC (figure 6(d)). This indicates that FCC phase has more excellent plastic deformation ability during the deformation process. It means that FCC matrix provide ductility, and boundaries between BCC phase and matrix contribute to strength.

4.2. μ-precipitation strengthen mechanism

We carefully characterized the microstructure evolution of the fractured samples, so as to reveal the plastic deformation mechanism of the material during the tensile process. In such a three-phase alloy, all phases participate in the strengthening. Among them, nano-sized precipitated μ-phase has the most significant effect in the strengthening mechanism. Firstly, we discuss the phasing mechanism of μ-phase in the deformation process. There are two main mechanisms of precipitation strengthening: the dislocation shearing of precipitates and the Orowan bypass mechanism [17–20]. Which of these two strengthening mechanisms will occur depends on many factors, including the size of precipitate, coherency or incoherency, and its structural features. In the W30Mo7FeNi alloy, the size of μ-phase particle is larger than 100 nm. And according to our previous studies, there is no coherent relationship between the μ phase and FCC matrix. Hence, the strengthening mechanism of μ phase is dislocation bypass mechanism, i.e. Orowan effect (figure 7(a)). During the deformation, the μ-phase significantly retards the dislocation motion. The dislocation is plugged at the interface between the μ phase and the FCC matrix (figure 7(a)). To further analyze the Orowan mechanism, the strength increment $\Delta\sigma_\mu$ can be calculated by [18, 19]:

$$\Delta\sigma_\mu = M\frac{0.4Gb}{\pi\sqrt{1-\nu}}\frac{\ln\left(2\sqrt{\frac{2}{3}}r/b\right)}{2\sqrt{\frac{2}{3}}r\left(\sqrt{\frac{\pi}{4f}}-1\right)}$$

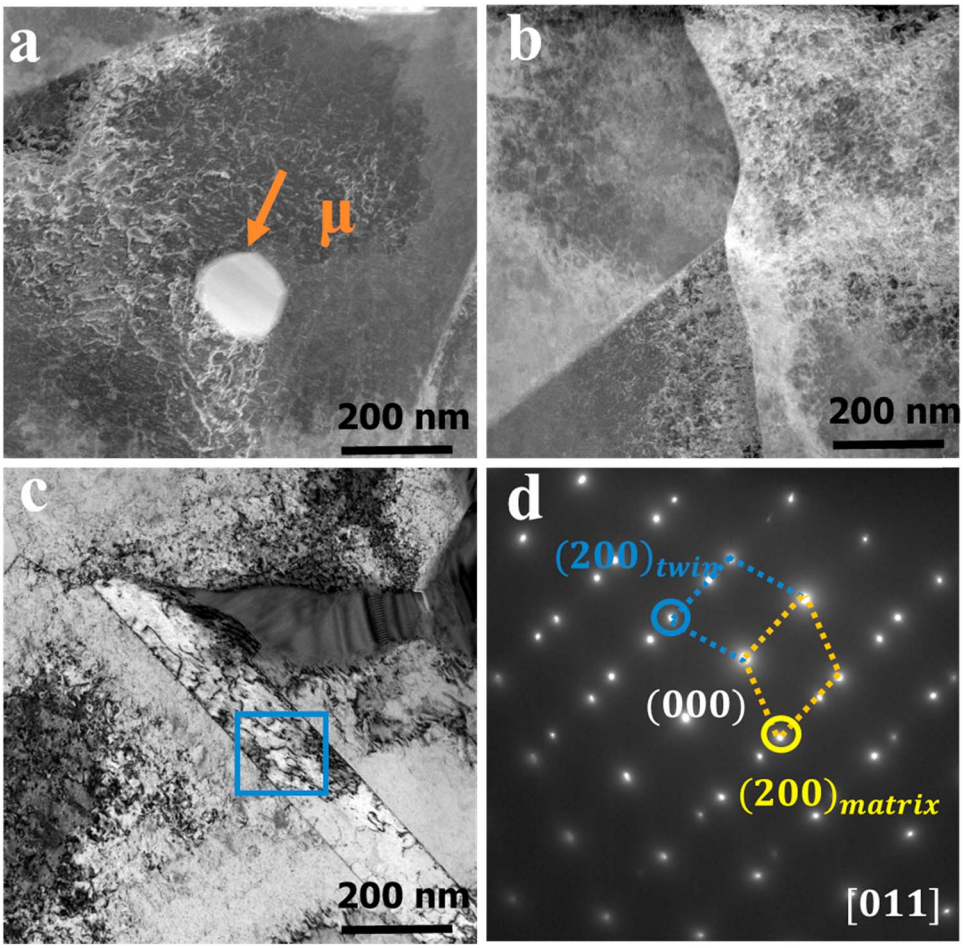

Figure 7. Microstructure of the aged alloy after tensile deformation. (a). HAADF image of dislocation pile up at μ particle. (b). HAADF image of dislocation plugged at the grain boundary. (c). Bright field TEM image shows that the dislocation interacts with the twin boundaries. (d). The SAED pattern of the red-colored rectangle region in c.

where $\nu = 0.3$ is the Poisson ratio; $r = 150$ nm is the average diameter of μ particles, , $M = 3.06$ is the Taylor factor, $G = 77$ GPa is the shear modulus, $b = \sqrt{2}$ a/2 is the Burgers vector, $f = 0.11$ is volume fraction. The strength increments were approximately 475 MPa.

4.3. Refined crystalline strengthen mechanism

In addition to μ phase precipitation, grain boundary strengthening is also an important reason for the improvement of the strength. Figure 7(b) shows the dislocation plugging at the grain boundary. The grain size of FCC phase was significantly reduced by recrystallization annealing. The grain size decreases from 400 μm to ~3 μm (figure 3), and even the grain size of local structure with ultrafine grains is less than 1 μm (figure 4(e)). Moreover, the presence of twin boundary due to the low stacking fault energy during recrystallization can also hinder the dislocation (figure 4(e) and figure 7(c)). According to the Hall-Petch effect, the strength increase caused by grain refinement ($\Delta\sigma_g$) can be estimated by the following equation [21–25]:

$$\Delta\sigma_g = K(d_2^{-0.5} - d_1^{-0.5})$$

where $d_1 = 400$ μm is the grain size of the as-cast alloy, $d_2 = 3$ μm are the grain size of aged alloy, and K = 296 MPa*μm$^{0.5}$ is the Hall–Petch grain-size hardening constant. Based on the above discussion, the strength increase due to grain refinement can be estimated to be about 156 MPa. Hence, the synergistic strengthening of the two types of nanoscale precipitate and grain refinement provides a prime contribution to the about 631 MPa strength of the W30Mo7FeNi HEA. A column chart and a table are summarized as shown in figure 8, which shows the estimated values agree well with the measured data. Thus, the theoretical prediction is highly consistent with the experimental results.

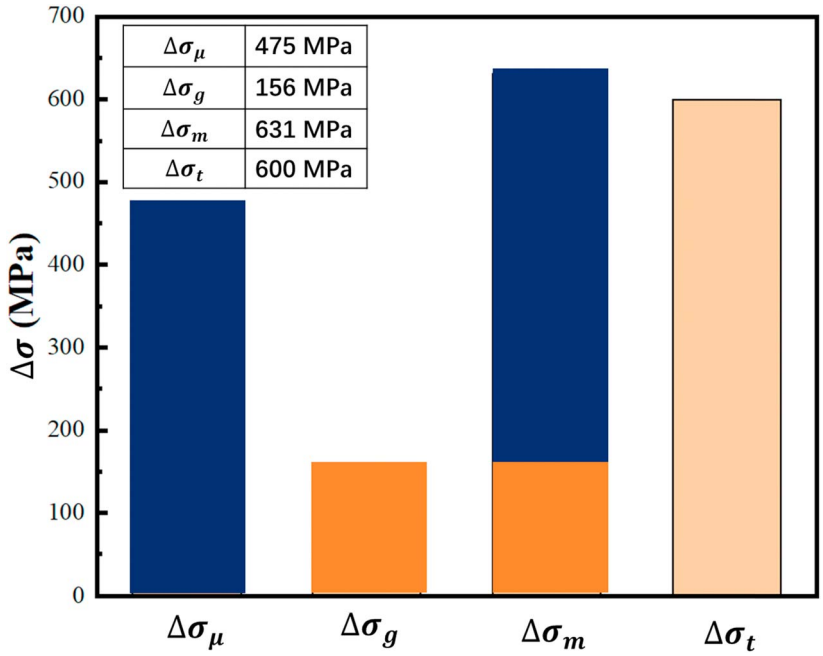

Figure 8. Contributions of different strengthening mechanisms, the μ-precipitation strengthen mechanism ($\Delta\sigma_\mu$), the refined grain strengthening ($\Delta\sigma_g$), the measured data ($\Delta\sigma_m$), and the true data ($\Delta\sigma_t$).

5. Conclusion

In summary, by tailoring the phase transformation process, we successfully eliminate the as-cast μ phase and significantly improve the workability of the self-sharping tungsten high-entropy alloy. Due to precipitation strengthening and grain refinement strengthening, the strength of the material is about 2 times higher than that of the as-cast alloy and achieves 950 MPa, while the tensile ductility is maintained. We believe that such design philosophy may provide a novel and highly effective approach for the future development of other advanced materials.

Acknowledgments

This work is supported by the NSFC (Nos. 11790292, 11972346, 12102433 and No. U2141204), the National Key Research and Development Program of China (No. 2017YFB0702003), the NSFC Basic Science Center Program for 'Multi-scale Problems in Nonlinear Mechanics' (No. 11988102), the Strategic Priority Research Program (No. XDB22040302 and No. XDB22040303), the Key Research Program of Frontier Sciences (Grant No. QYZDJSSW- JSC011), Science Challenge Project (No. TZ2016001), the Key Research Program of the Chinese Academy of Sciences (Grant No. ZDRW-CN-2021–2–3), and the opening project of State Key Laboratory of Explosion Science and Technology (Grant No. KFJJ21–01Z).

Data availability statement

All data that support the findings of this study are included within the article (and any supplementary files).

Competing interests

Authors declare that they have no competing interests.

ORCID iDs

Lanhong Dai https://orcid.org/0000-0001-8991-0358

References

[1] Magness L S 1994 High strain rate deformation behaviors of kinetic energy penetrator materials during ballistic impact **17** 147–54
[2] Liu T W, Li T and Dai L H 2022 Near-equiatomic μ phase in self-sharpening tungsten-based high-entropy alloys *Metals* **12** 1130
[3] Liu X F *et al* 2020 'Self-sharpening' tungsten high-entropy alloy *Acta Mater.* **186** 257–66
[4] Luo R *et al* 2016 Materials science & engineering a penetrating performance and 'self-sharpening' behavior of fi ne- grained tungsten heavy alloy rod penetrators *Mater. Sci. Eng.* A **675** 262–70
[5] Arfsten D P, Still K R and Ritchie G D 2001 A review of the effects of uranium and depleted uranium exposure on reproduction and fetal developmentt *Toxicol. Ind. Health* **17** 180–91
[6] Cantor B *et al* 2004 Microstructural development in equiatomic multicomponent alloys *Mater. Sci. Eng.* A **375** 213–8
[7] Yeh J W *et al* 2004 Nanostructured high-entropy alloys with multiple principal elements: novel alloy design concepts and outcomes *Adv. Eng. Mater.* **6** 299–303
[8] Li T *et al* 2023 Ultra-strong tungsten refractory high- entropy alloy via stepwise controllable coherent nanoprecipitations *Nat. Commun.* **14** 3006
[9] Li C *et al* 2021 New TiTaNbZrMo high-entropy alloys for metallic biomaterials *Mater. Res. Express* **8** 105403
[10] Jinlong L and Jin. H 2020 Corrosion resistance mechanism of the passive films formed on as- cast FeCoCrNiMn high-entropy alloy *Nature Materials, Mater. Res. Express* **7** 016592
[11] Senkov O N *et al* 2010 Refractory high-entropy alloys *Intermetallics* **18** 1758–65
[12] Senkov O N *et al* 2011 Mechanical properties of Nb25Mo25Ta 25W25 and V20Nb20Mo 20Ta20W20 refractory high entropy alloys *Intermetallics* **19** 698–706
[13] Zhang Y *et al* 2014 Microstructures and properties of high-entropy alloys *Prog. Mater Sci.* **61** 1–93
[14] George E P, Raabe D and Ritchie R O 2019 High-entropy alloys *Nature Reviews Materials* **4** 515–34
[15] Zhao S *et al* 2021 Amorphization in extreme deformation of the CrMnFeCoNi high-entropy alloy *Sci. Adv.* **7** 1–7
[16] Yang T *et al* 2018 Multicomponent intermetallic nanoparticles and superb mechanical behaviors of complex alloys *Science* **362** 933–7
[17] Zhou T *et al* 2019 Effect of precipitates on high-temperature tensile strength of a high W-content cast Ni-based superalloy *J. Alloys Compd.* **797** 486–96
[18] Xiang S *et al* 2016 Selective evolution of secondary γ' precipitation in a Ni-based single crystal superalloy both in the γ matrix and at the dislocation nodes *Acta Mater.* **116** 343–53
[19] Sundararaman M, Mukhopadhyay P and Banerjee S 1988 Precipitation of the δ-Ni3Nb phase in two nickel base superalloys *Metall. Trans.* A **19** 453–65
[20] Jiao Z B *et al* 2017 Co-precipitation of nanoscale particles in steels with ultra-high strength for a new era *Mater. Today* **20** 142–54
[21] Gao J *et al* 2021 Facile route to bulk ultrafine-grain steels for high strength and ductility *Nature* **590** 262–7
[22] Yoshida S *et al* 2019 Acta Materialia Effect of elemental combination on friction stress and hall-petch relationship in face-centered cubic high / medium entropy alloys *Acta Mater.* **171** 201–15
[23] Yoshida S *et al* 2017 Friction stress and hall-petch relationship in CoCrNi equi-atomic medium entropy alloy processed by severe plastic deformation and subsequent annealing *Scr. Mater.* **134** 33–6
[24] Chen S *et al* 2019 Grain growth and hall-petch relationship in a refractory HfNbTaZrTi high-entropy alloy *J. Alloys Compd.* **795** 19–26
[25] Sansoz F and Ke X 2022 Acta materialia hall—petch strengthening limit through partially active segregation in nanocrystalline Ag-Cu alloy *Acta Mater.* **225** 117560